Controls on surface warming by polar clouds in idealized large-eddy simulations

Antonios Dimitrelos,[a] Rodrigo Caballero[a] and Annica M.L. Ekman[a].

[a] *Department of Meteorology and Bolin Centre for Climate Research, Stockholm University, Stockholm, Sweden*

Corresponding author: Antonios Dimitrelos, antonios.dimitrelos@misu.su.se

This paper is a non-peer reviewed preprint submitted to EarthArXiv

This paper is submitted to the Journal of Climate

ABSTRACT

The main energy input to the polar regions in winter is the advection of warm, moist air from lower latitudes. This makes the polar climate sensitive to the temperature and moisture of extra-polar air. Here, we study this sensitivity from an air-mass transformation perspective. We perform simulations of an idealized maritime air mass brought into contact with sea ice employing a three-dimensional large-eddy simulation model coupled to a one-dimensional multilayer sea ice model. We study the response of cloud dynamics and surface warming during the air-mass transformation process to varying initial temperature and humidity conditions of the air mass. We find in all cases that a mixed-phase cloud is formed, initially near the surface but rising continuously with time. Surface warming of the sea ice is driven by downward longwave surface fluxes, which are largely controlled by the temperature and optical depth of the cloud. Cloud temperature, in turn, is robustly constrained by the initial dewpoint temperature of the air mass. Since dewpoint only depends on moisture, the overall result is that surface warming depends almost exclusively on initial humidity and is largely independent of initial temperature. We discuss possible climate implications of this result, in particular for polar amplification of surface warming and the role played by atmospheric energy transports.

1. Introduction

A fundamental feature of the climate system's response to global radiative forcing is that surface warming is enhanced at the poles relative to lower latitudes, a phenomenon known as polar amplification. A variety of mechanisms is understood to contribute to polar amplification—most notably surface albedo feedback, temperature structure feedbacks, and changes in poleward energy transport—but there is ongoing debate about the precise functioning of these mechanisms, their mutual interaction and their relative contribution to polar amplification (see reviews by Goosse et al. 2018 and Previdi et al. 2021). Particular uncertainty surrounds the role played by clouds: a survey of recent literature shows as many studies indicating a positive as a negative or ambiguous contribution to polar amplification by cloud feedbacks (Previdi et al. 2021). This uncertainty partly reflects the complex structural and microphysical characteristics of polar clouds (Curry et al. 1996), which are poorly captured by conventional climate models (Pithan et al. 2014, 2016) even in their "superparameterized" versions (Li and Xu 2020).

Polar amplification is strongest in winter, and clouds are observed to have a strong surface warming effect in that season and also in the annual mean (Kay et al. 2016). Low-level mixed-phase clouds are particularly important for this warming effect. Such clouds are abundant in the Arctic (Shupe 2011) and are observed to persist for many days despite the coexistence of liquid and ice phases (Morrison et al. 2012). Observations show that the phases tend to segregate into distinct layers: a relatively thin top layer containing mostly supercooled liquid condensate, and a deeper layer underneath where ice condensate predominates (Morrison et al. 2012). The top layer makes the clouds opaque to longwave radiation when the liquid water path exceeds 30 g m^{-2} (Shupe and Intrieri 2004). Given their low elevation and relatively warm temperature, the presence of optically-thick mixed-phase clouds warms the surface by intensifying downward longwave radiation: when clear skies are replaced by low clouds over sea ice in winter, the surface is observed to warm by 10–20˚C (Stramler et al. 2011, Persson et al. 2017). The optically-thick cloud top can also generate enough radiative cooling to drive top-down convection that helps maintain the liquid condensate layer (Curry 1986). Moreover, humidity inversions at cloud top resupply the cloud with vapor through turbulent entrainment even when the cloud is decoupled from the surface by a shallow surface-based inversion (Solomon et al. 2011, Dimitrelos et al. 2020).

Arctic low clouds form under specific synoptic-scale conditions, in particular when relatively warm, moist maritime air is advected over sea ice or land (Persson et al. 2017). These advection events take the form of filamentary structures referred to as moist intrusions (Doyle et al. 2011) that penetrate deep into the Arctic Ocean basin. Intense moist intrusions occur about once per week on average in winter, most commonly entering the Arctic from the Atlantic sector and taking around 5 days to cross the basin before exiting over northwestern Canada or Alaska (Woods and Caballero 2016). Interannual fluctuations in the statistics of moist intrusions—or more generally in the moisture influx into the Arctic—drive variability and trends in seasonal-mean downward longwave radiation, surface temperature and sea ice cover (Woods et al. 2013, H.-S. Park et al. 2015, D.-S. R. Park et al. 2015, Woods and Caballero 2016, Gong et al. 2017).

Air masses involved in moist intrusions originate over the open ocean, with the typical temperature, moisture and stratification of midlatitude or subpolar marine air. Once they make contact with sea ice or land in winter, they are cut off from their surface energy and moisture source. Longwave cooling promotes cloud formation, and the clouds formed eventually dissipate once liquid or ice precipitation depletes the initial stock of humidity. The end result is a cold, dry, cloud-free Arctic air mass. As argued in Pithan et al. (2018), a full understanding of the Arctic climate cannot be separated from an understanding of this air-mass transformation process. Because the process is intrinsically Lagrangian, occurring as the air mass travels large distances, it is difficult to observe directly using ground-based systems, while the sampling frequency of polar-orbiting satellites is insufficient to capture the timescales involved. Idealized column model studies of the process have a long history (Wexler 1936, Curry 1983, Cronin and Tziperman 2015, Pithan et al. 2016) and highlight the complexity of the interactions between cloud dynamics, microphysics and radiation, and the difficulty in capturing them using conventional parameterizations.

Here, we aim to deepen our understanding of how a warming and moistening of lower-latitude marine air affect Arctic clouds and their surface impacts. To capture the relevant processes with as much realism as possible, we use a high-resolution, fully three-dimensional large eddy simulation (LES) model with a sophisticated description of cloud microphysics, coupled to a multilayer sea ice model. For consistency with previous work, we adopt a column pseudo-Lagrangian framework (Cronin and Tziperman 2015, Pithan et al. 2016). For simplicity, and because Arctic warming is greatest in winter, we focus on polar night conditions. Details of the model and simulation setup are provided in Section 2 and the Appendix.

Specifically, we address the question of how the initial temperature and initial humidity of air flowing into the Arctic separately affect the subsequent cloud evolution and surface impacts during the air-mass transformation process. One might naively assume that, for a given humidity, a warmer air mass would produce greater surface warming—both by producing warmer clouds with greater surface radiative impact, and by enhancing sensible heat flux into the ice. Our key result, presented in Section 3, is that this assumption is incorrect: initial temperature makes little difference to surface warming, which is controlled exclusively by initial humidity. As discussed in Sections 4 and 5, the main reason for this behavior is that cloud and sub-cloud temperatures are tightly constrained by the air mass's initial dewpoint temperature, which depends only on its humidity. In Section 6 we summarize our conclusions and discuss their potential implications for Arctic climate and polar amplification.

2. Methods

a. Large-eddy simulation model: MIMICA

MIMICA (Savre et al. 2014) is a three-dimensional LES model that uses a 1.5 order subgrid-scale turbulence closure scheme. The surface turbulent fluxes are calculated using Monin-Obukhov similarity theory (Garrat 1994). The model includes a two-moment bulk microphysics scheme, where prognostic equations for the mass mixing ratio and number concentration of hydrometeors are solved. Five types of hydrometeors are considered: cloud droplets, raindrops, pristine ice crystals, snow, and graupel. In this study, the snow and graupel categories are excluded, since we found that aggregation, riming and accretion did not affect the results. The size distributions of the hydrometeors are prescribed by gamma functions (Savre et al. 2014) and their terminal fall speeds are described by simple power laws (Pruppacher and Klett 1997). The ice crystal habit was defined to be plate, in agreement with the cloud layer temperatures obtained during the simulations. The warm microphysics interactions are parameterized according to Seifert and Beheng (2001) and the supersaturation is explicitly calculated at every model time step (Morrison and Grabowski, 2008). The number of activated cloud condensation nuclei (CCN) is calculated as in Khvorostyanov and Curry (2005) and all CCN are assumed to consist of ammonium sulfate. The number concentration of the CCN is held constant throughout the simulations. The ice crystal number concentration is relaxed towards a fixed background value according to Morrison et al. (2011). A multiband 2-4 stream radiative solver is used to calculate the radiative flux densities (Fu and Liou 1993). The radiative solver takes into account the mixing ratio of all hydrometeor types. Prescribed vertical profiles of parameters that describe the atmosphere are used to calculate radiative fluxes from the domain top to the top of the atmosphere. Lateral boundary conditions are periodic and a sponge layer is applied at the domain top to damp any gravity waves. For the simulations in this study, the length and width of the domain is set to 6 km, while its vertical extent is 4 km. The horizontal grid spacing is set to 62.5 m, and the vertical grid is split into two zones. The layer from the surface up to 2.5 km has a resolution of 15 m. The upper part of the domain has a higher resolution of 7.5 m. This grid division prevents numerical instabilities originating from gravity waves formed at cloud top when the cloud dissipates, which occurs at heights above 2.5 km.

b. Sea ice model

A 1-dimensional thermodynamic sea ice model was developed and coupled to MIMICA in order to study the surface and subsurface warming effect of the clouds. The model is an upgraded version of that used in Dimitrelos et al. (2020), which was a one-layer slab sea ice model. Here, the sea ice model includes four layers to better represent heat conduction within the sea ice and energy exchange with the atmosphere. The surface layer is assumed to be snow while the underlying layers are ice of different characteristics. A schematic of the model is presented in Figure 1. The model solves energy balance equations at the layer interfaces and heat conduction within the layers. A detailed description of the model equations and parameter values is provided in the Appendix.

The atmosphere and sea ice interact through the surface energy balance equation

$$F_{LWd} - F_{LWu} + F_{SH} + F_{LH} + F_C = 0, \qquad (1)$$

where F_{LWd} and F_{LWu} are surface downward and upward longwave fluxes respectively, F_{SH} and F_{LH} are turbulent sensible and latent heat fluxes, described through a bulk aerodynamic approximation (see Appendix) and F_C is the surface conductive flux, which depends on the temperature difference between the surface and the underlying snow layer. Horizontal-mean values of near-surface air properties and radiative fluxes are used as fluxes into the sea ice model, while the surface temperature and upward fluxes computed by the sea ice model are provided as input to the atmospheric model uniformly at all grid points. Note that solar radiative fluxes are absent as our simulations target polar night.

An initial sea ice temperature profile is defined through an offline simulation of the sea ice model with F_{LWd} fixed at 170 W m^{-2} (matching observed clear-sky values in the high Arctic, Persson et al. 2017) while the air temperature at 10 m altitude is set to be 0.5˚C warmer than the surface temperature, yielding surface turbulent fluxes ~1 W m^{-2}. The sea ice model is run under these conditions until all layers reach the steady-state temperature profile shown in Figure 1b. In this state, surface temperature is –30˚C, net longwave radiative flux $F_{LWd} - F_{LWu}$ = –12 W m^{-2} while F_C = 11 W m^{-2}.

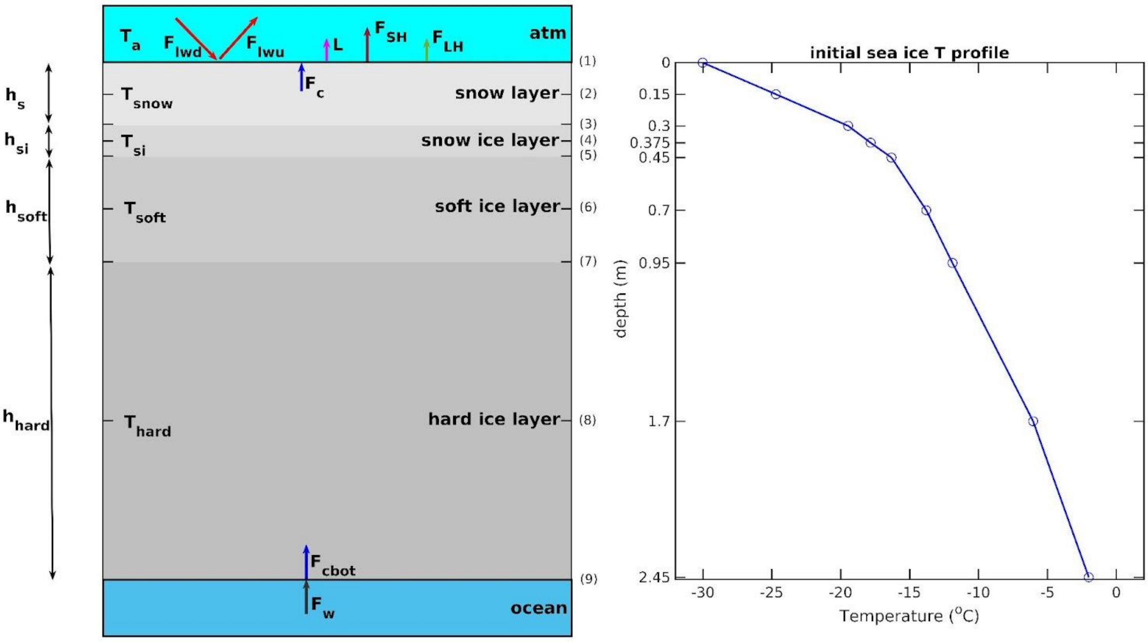

Fig. 1. (Left) Schematic of the sea ice model. Symbol definitions and a detailed description of the model is provided in the Appendix. (Right) Initial temperature profile in the sea ice model.

c. Simulation setup

Each simulation is initialized with a specified atmospheric temperature and humidity profile (described below), in contact with the initial ice temperature profile shown in Figure 1. The LES model is then allowed to evolve freely, exchanging energy with the surface but with no externally-imposed lateral boundary fluxes (the flow is re-entering at the lateral boundaries). This setup, common to previous work (e.g. Cronin and Tziperman 2015, Pithan et al. 2016), aims to capture the air-mass transformation process in a quasi-Lagrangian fashion, i.e. following an initially warm, moist maritime air column as it is advected over sea ice. There are obvious limitations to the realism of this approach: an advected air column will in reality continuously encounter unperturbed sea ice, rather than always interacting with the same sea ice as in our simulations. Also, a real air column will generally be deformed by large-scale wind shear rather than conserve its vertical coherence. Nonetheless, we employ this approach in the interest of simplicity and for consistency with previous work.

In all simulations, the initial atmospheric temperature profile takes the form $T = T_0 - \Gamma z$, where z is height and the lapse rate $\Gamma = 8^{\circ}\mathrm{C\ km^{-1}}$ in all cases. The relative humidity profile takes the same form, $\mathrm{RH} = \mathrm{RH}_0 - \Gamma_{RH}\, z$, with $\Gamma_{RH} = 15\%\ \mathrm{km^{-1}}$. The simulations are distinguished only by the initial surface values T_0 and RH_0. We perform simulations with all combinations of three T_0 values (0, 5 and 10˚C) and three RH_0 values (70, 80 and 90%), for a total of nine simulations. These values are chosen to roughly capture typical subpolar maritime conditions in the modern and warmer future climates. We use the notation T0RH70 to refer to the simulation with T_0 = 0˚C and RH_0 = 70%.

A further set of six simulations was designed to test the sensitivity to changing initial *specific* humidity at fixed initial temperature and vice-versa. Three of these simulations (denoted T0Lo, T5Lo and T10Lo) have initial T_0 = 0, 5 and 10˚C respectively but all have the same initial specific humidity profile as in T0RH90. The other three (T0Hi, T5Hi and T10Hi) all have the higher initial specific humidity profile of T5RH90. Note that T0RH90 is actually the same as T0Lo while T5Hi is the same as T5RH90; also, the T0Hi simulation was omitted as its initial temperature and humidity values imply supersaturation. We thus have a total of 12 distinct simulations.

In all simulations, the sea ice model is initialized with the temperature profile in Figure 1b. All simulations are initially cloud-free and assume a fixed number concentration of CCN (30 cm^{-3}) and ice nuclei (1 $liter^{-1}$). An initial vertically uniform mean horizontal wind of 5 m s^{-1} is applied to all experiments, and the winds are nudged to their initial value throughout the simulation. All simulations assume zero divergence and large-scale subsidence. Shortwave radiation is zero in all cases as we are assuming polar night. Each simulation is run for 5 days.

3. Surface warming response

Figure 2a plots the time-mean surface temperature T_s over the 5-day duration of each simulation as a function of the initial surface specific humidity q_0. Depending on the initial atmospheric conditions, the surface warms by 5–25˚C above its initial temperature of –30˚C over the course of the air-mass transformation process. This magnitude of warming is consistent with surface temperature anomalies typically observed during moist intrusion events in the wintertime high Arctic (Woods and Caballero 2016, Messori et al. 2018).

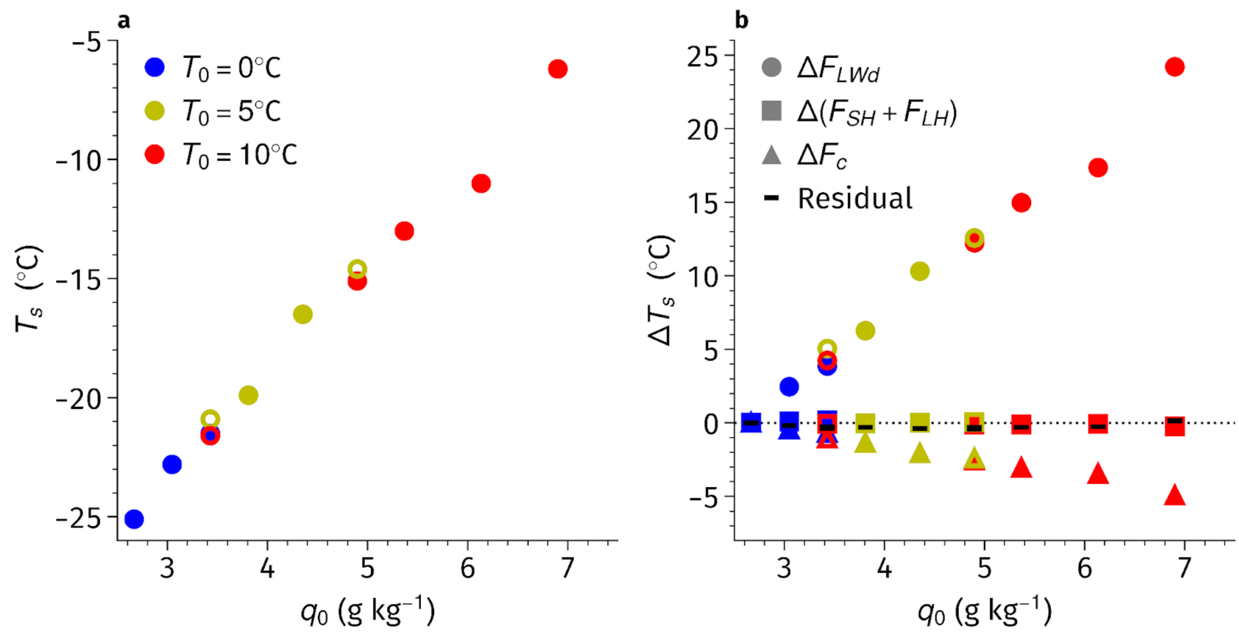

Fig. 2. (a) Time-mean surface temperature T_s as a function of initial surface specific humidity q_0 for all simulations. (b) Decomposition of the surface temperature response into contributions from downward longwave flux (circles), turbulent fluxes (squares) and conductive flux (triangles), see Equation (2) in text. Values are plotted as differences from the reference case T0RH70. The residual (thick black dashes) is the difference between ΔT_s derived using (2) and the actual ΔT_s in the simulations. Colors indicate the initial air surface temperature T_0 (see legend in panel a). Open symbols indicate the T5Lo, T5Hi and T10Lo cases.

Importantly, Figure 2a shows a roughly linear dependence of surface warming on initial humidity, suggesting a central role for humidity in controlling surface impacts. This is confirmed by noting that simulations with the same initial specific humidity but different initial temperatures have very similar surface warming: specifically, T0Lo, T5Lo, and T10Lo (which all have initial q_0 of around 3.5 g kg^{-1}) all result in T_s of about –21˚C, while T5Hi and T10Hi ($q_0 \approx 5$ g kg^{-1}) both yield T_s of around –15˚C. It therefore appears that the surface temperature response—at least in the time-mean—is controlled almost entirely by the initial specific humidity, with initial temperature playing a negligible role. Put another way, two air-mass transformation processes starting with the same relative humidity but different temperatures have different surface impacts only by virtue of their different specific humidity, not directly because of their different temperature.

To gain insight into the proximate causes for the surface temperature response, we decompose the surface temperature response into contributions from different surface flux terms by linearising the surface energy balance Equation (1) around a reference surface temperature (Lee et al. 2017):

$$\Delta T_s \approx (\Delta F_{LWd} + \Delta F_{SH} + \Delta F_{LH} + \Delta F_C)/4\epsilon\sigma T_s^3, \quad (2)$$

where ΔT_s is the difference in time-mean T_s between a given simulation and a reference simulation (taken as T0RH70, our coldest and driest case). Differences in downward longwave radiative flux ΔF_{LWd}, turbulent sensible and latent heat fluxes ΔF_{SH} and ΔF_{LH}, and conductive heat flux ΔF_C at the surface (again time-averaged over the first 5 days of each simulation) are computed in a similar manner. Figure 2b shows the terms on the r.h.s. of (2) for each simulation. The residual in (2), i.e. the difference between the sum of the four terms on the r.h.s. and the model-produced ΔT_s is very small, implying that (2) provides an adequate approximation.

Figure 2b shows that the longwave and conductive terms scale roughly linearly with initial humidity, while the turbulent flux terms change little across the simulations. The only positive term is downward longwave radiation, which is therefore the sole driver of increased surface warming with increasing humidity, and is only partly offset by the increasingly negative conductive term, i.e. by increased cooling of the surface through heat transfer into the underlying snow and ice. The dominant role of downward longwave radiation in driving surface temperature change is consistent with observational work over pack ice in winter (e.g. Lee et al. 2017). Cases with the same initial specific humidity show very similar values of ΔF_{LWd}, ΔF_{SH} and ΔF_C, so initial humidity is the dominant control not just on the overall surface temperature response, but on individual surface energy budget terms as well.

4. Cloud dynamics and the role of initial dewpoint temperature

To better understand the results of the previous section, we select three specific simulations for closer examination: two with equal initial air temperature but different initial humidity (T5Lo and T5Hi), and another, T10Lo, with the same initial humidity as T5Lo but higher initial temperature. These simulations are indicated by open symbols in Figure 2.

Figure 3 shows the time evolution of surface temperature and downward longwave flux in the three simulations. Comparing Figures 3a and 3b, it is clear that surface temperature closely tracks the downward longwave flux not just in the time mean, as shown in the previous section, but at every instant. Since we expect downward longwave radiation to be heavily influenced by the presence and nature of clouds in the air column, we devote the rest of this section to an analysis of cloud evolution during the simulations.

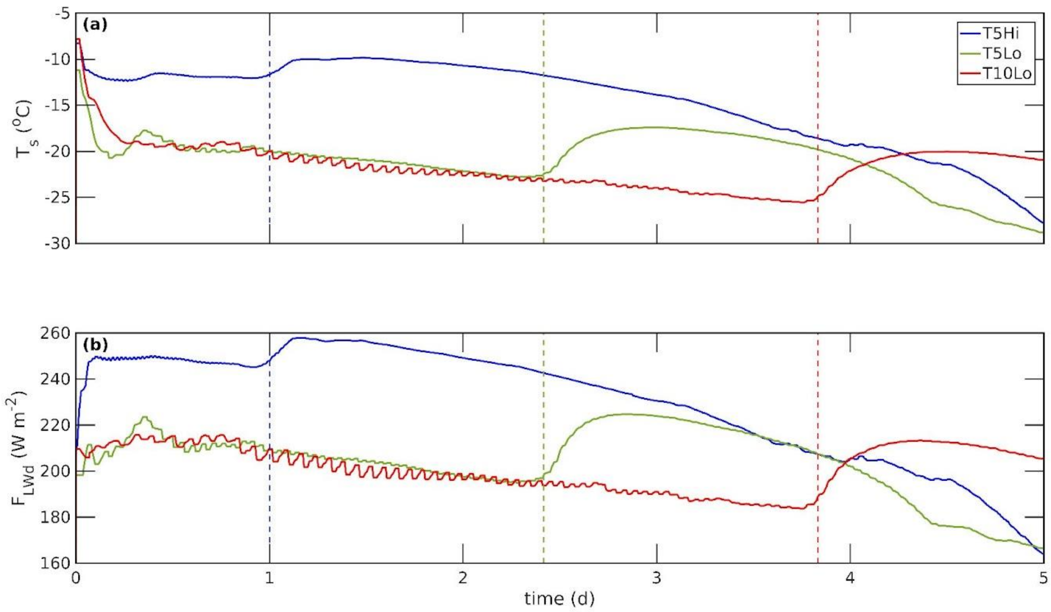

Fig. 3. Time evolution of horizontally-averaged (a) surface temperature T_s and (b) surface downward longwave flux F_{LWd} for T5Hi (blue lines), T5Lo (green) and T10Lo (red). Vertical dashed lines in corresponding colors mark the transition from the stable to the convective regime.

a. Cloud regimes

Figure 4a-c presents the time evolution of cloud condensate in the three simulations. All three exhibit cloud tops initially near ground level but steadily rising throughout the 5 day period. This behavior is common to all simulations conducted in the present study. Note that the cloud elevates most rapidly in the moister case T5Hi, while among the two drier cases it rises fastest in the initially colder one (T5Lo). We examine the reasons for these different elevation rates below.

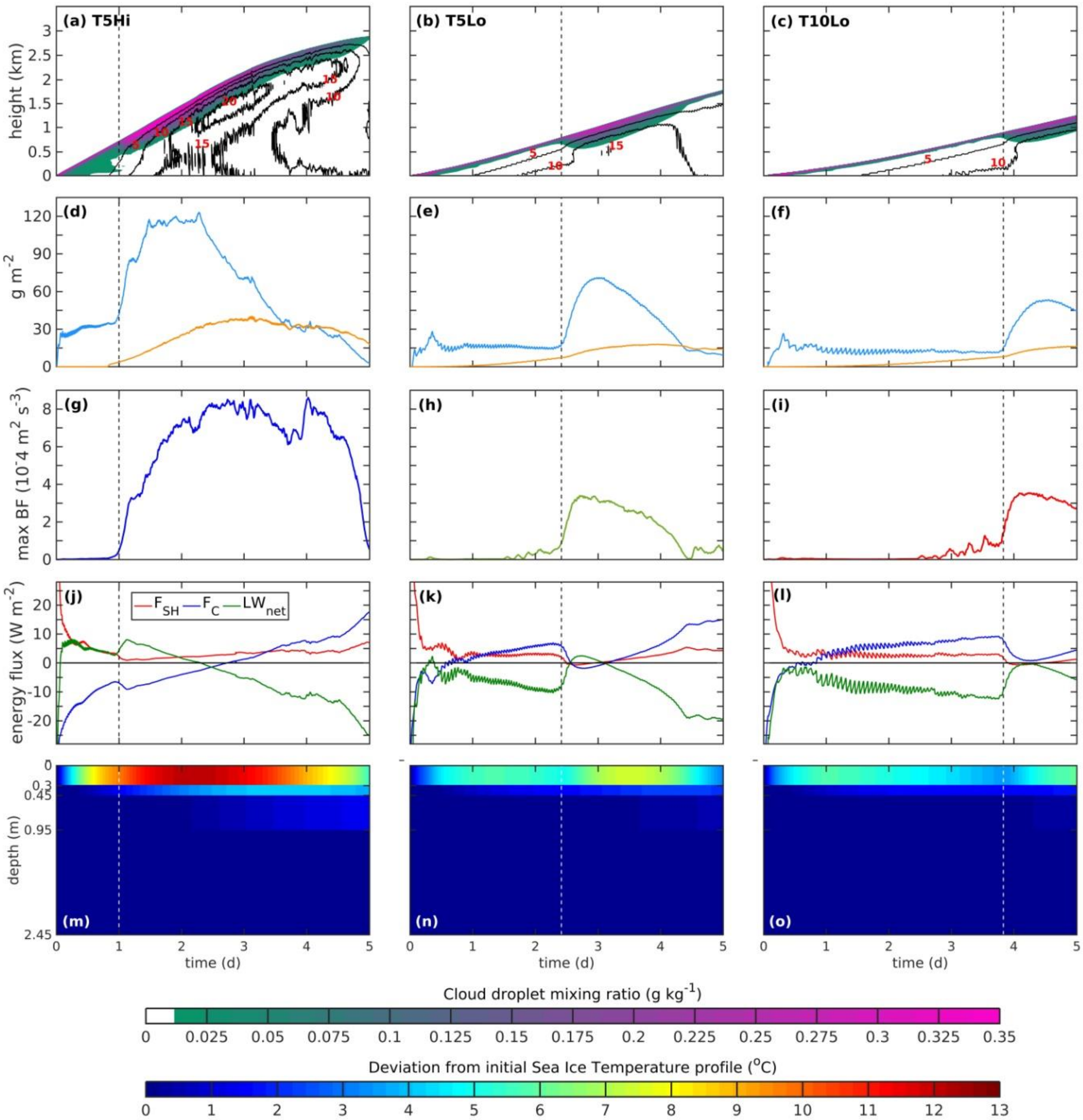

Fig. 4. Time evolution of horizontal-mean (a-c) cloud liquid water mixing ratio (shading) and ice crystal mixing ratio (contours at intervals of 5 g kg^{-1}); (d-f) liquid water path (blue line) and ice water path (yellow); (g-i) maximum value of horizontally-averaged turbulent buoyancy flux; (j-l) surface net longwave flux (green lines), sensible heat flux (red) and conductive flux (blue); (m-o) mid-layer temperatures in the ice model, shown as the difference from the initial temperature profile (Figure 1b). Dashed vertical lines in each panel denote the transition from the stable to the convective regime. Left, middle and right columns show results for T5Hi, T5Lo and T10Lo respectively.

Another feature common to all three cases is that buoyancy-driven turbulence (as measured by the maximum positive turbulent buoyancy flux, Figure 4g-i) is initially near zero, transitioning sharply to larger values only some time into the simulations. We can therefore distinguish two distinct stages of cloud evolution: an initial stable, non-convective regime, followed by a turbulent convective regime. For reference, dashed lines in Figure 3 show the approximate time at which this transition occurs in each simulation. In the late stages of the simulations, the buoyancy flux decreases to near-zero once again as the cloud dissipates, and we can distinguish a third, decay stage (visible for T5Hi and T5Lo, but a longer simulation would be required to capture it in T10Lo). We focus below on the stable and convective regimes.

Profiles of ice-liquid-water potential temperature at different times in the simulations (Figure 5a-c) show that the entire column is indeed statically stable during the stable regime, but in the convective regime it becomes neutrally stable within a layer immediately below the cloud, remaining strongly stable near the surface. The convective regime profiles are consistent with vigorous convection driven by cloud-top radiative cooling and mixing below the cloud, yielding the neutrally-stable profile there, but convection does not penetrate all the way to the ground because of strong near-surface stability. We can thus characterize the convective regime as a stratocumulus-topped convective layer overlying a decoupled surface layer, a regime well known from previous observational and modeling studies of polar clouds (Shupe et al. 2013; Solomon et al. 2011; Svensson and Mauritsen 2020). The stable state with a fog or thin stratus cloud is less well characterized observationally, though fogs or very low, thin stratus are often observed near the sea ice margin (Sotiropoulou et al 2016). The overall cloud evolution, starting with a fog or thin stratus rising and transitioning to a deeper cloud structure, is also consistent with case studies of Arctic air-mass transformations tracked with Lagrangian tracers in reanalysis (You et al. 2021).

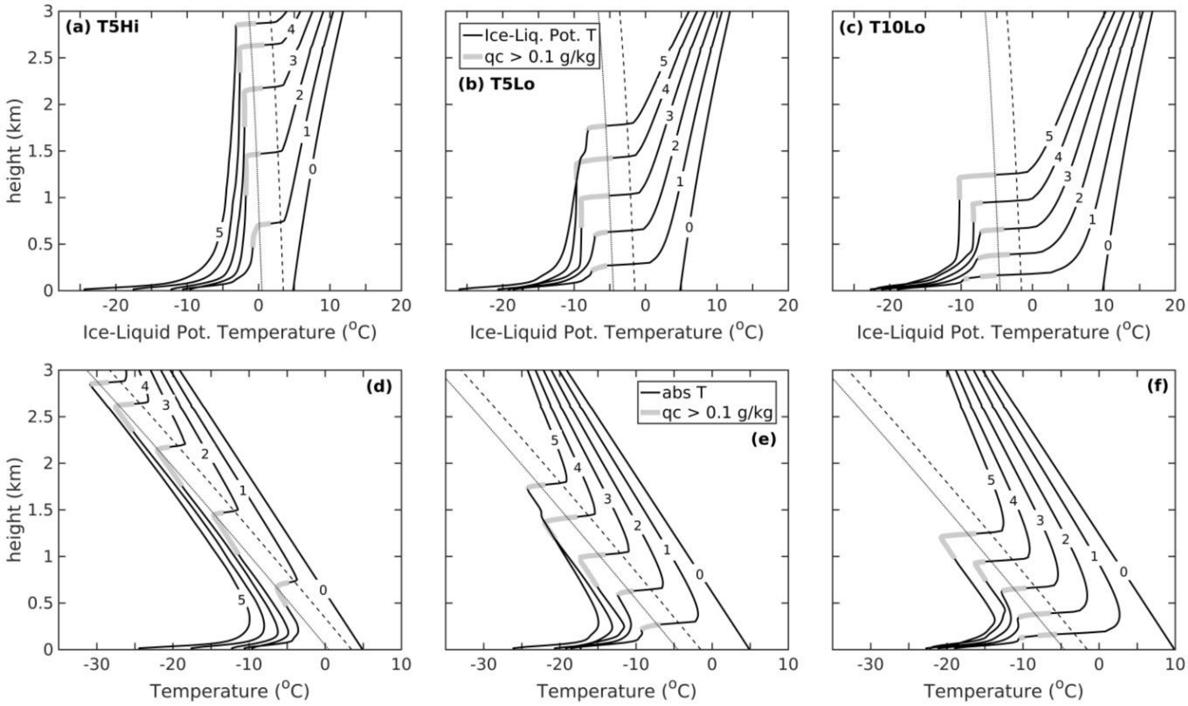

Fig. 5. Profiles of horizontal-mean ice-liquid potential temperature (top row) and absolute temperature (bottom) at selected times; numbers within each line show time in days from the start of each simulation. Gray shading indicates cloud (liquid water mixing ratio larger than 0.1 g kg^{-1}). Thin dashed lines show (a-c) initial dewpoint ice-liquid potential temperature and (d-f) initial dewpoint temperature. Thin solid lines show the corresponding profile minus 3˚C. Left, middle and right columns show results for T5Hi, T5Lo and T10Lo respectively.

The fact that the cloud top continuously rises in the convective regime is readily explained through cloud-top entrainment: since there is no large-scale subsidence in these simulations we expect the cloud top to rise at a speed set by the entrainment velocity (Mellado 2017). In the stable regime on the other hand, convection—and therefore entrainment—is absent, so the mechanism for cloud top elevation is less clear.

b. The stable regime

We propose the following conceptual picture for the evolution of the stable regime. In the initial clear-sky state, atmospheric radiative and sensible cooling maximizes near the surface, and near-surface air cools rapidly until its temperature drops below the dewpoint. A cloud (or fog) then forms and further cooling is slowed by latent heat release. This cloudy layer becomes opaque to longwave radiation, shifting the radiative cooling peak upward to the interface with the overlying clear air. The clear-air layer just above the cloud top then cools below its dewpoint and becomes cloudy; once sufficient condensate has formed to render it opaque, radiative cooling again shifts upwards and the whole process repeats in the layer above. As a result, cloud top in the stable regime rises in a layer-by-layer process controlled only by the local radiative cooling and latent heating within each layer.

Support for this conceptual picture is provided by Figure 6a, which shows the time-integrated radiative cooling and latent heating after 40 hours of the T5Lo simulation. The combined effect of these two tendencies yields a temperature profile that closely matches the actual simulated profile except near the surface. This close match implies that the sub-cloud temperature structure in the stable regime is determined almost entirely by local radiation and latent heat release, with no role for turbulent mixing except near the surface, where mechanical turbulence generates sensible heat flux from the atmosphere toward the colder surface below.

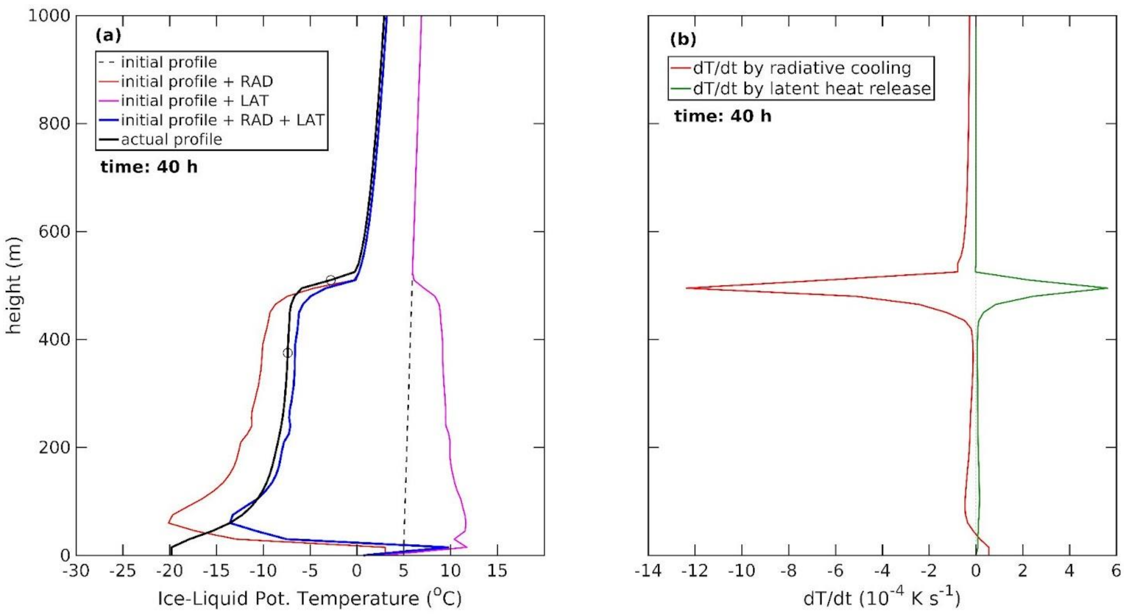

Fig. 6. Example of the roles played by radiative cooling and condensational heating in determining the atmospheric temperature profile. (a) Horizontal-mean ice-liquid potential temperature profile after 40 hours in the T5Lo simulation (black solid line), compared with the profile that would result if radiative cooling had acted alone (red line), if latent heating had acted alone (magenta line), and if the sum of radiative and latent heating had acted alone (blue

line). Thin dashed line displays the initial ice-liquid potential temperature. Circles mark cloud top and base. (b) Instantaneous horizontal-mean radiative cooling rate (red line) and latent heating rate (green line) at t = 40 hours in the T5Lo simulation.

In the absence of precipitation, the entire layer from cloud top to surface in the stable regime would be filled with cloud condensate. However, the simulations all exhibit substantial drizzle during the stable regime, which rapidly depletes cloud condensate and dissipates the cloud except in the thin layer where cloud formation is actively occurring. The resulting cloud is thus thin, filling a layer of only ~100 m thickness (Fig. 4a-c) with a liquid water path of 20–30 g m^{-2} (Fig. 4d-f).

The picture outlined above has several implications. The most important is that cloud temperature is, to a first approximation, determined by the dewpoint temperature of the initial maritime air mass. Both radiative cooling and latent heating rates drop to near-zero below the cloud, as shown in Figure 6b. The temperature in a given layer will therefore remain close to its value at the time of cloud formation, even after the cloud has shifted upward. Thus the entire sub-cloud temperature structure—except near the surface, where cooling by sensible heat flux divergence is important—remains close to the original dewpoint temperature profile. This fact is highlighted in Fig. 5d-f, where dashed lines show the initial dewpoint temperature and thin solid lines show a temperature profile 3˚C colder than the dewpoint; the latter gives a reasonable match to cloud temperature throughout the simulation in all cases.

We can therefore interpret the air mass transformation process during the stable regime simply as a readjustment of the sub-cloud temperature to a profile matching the initial dewpoint profile but shifted a few degrees colder. The initial temperature profile is in this sense irrelevant, since the dewpoint is controlled only by initial humidity. This helps explain why the surface temperature impact in our simulations (Figure 2) is controlled only by initial humidity while initial temperature plays a marginal role.

Initial temperature does play a role however in controlling the rate of ascent of the cloud: for a given initial humidity, a warmer initial temperature will need to cool for a longer time to reach the dewpoint; hence the slower rate of ascent in the T10Lo simulation than in T5Lo. Initial temperature also controls the strength of the cloud-top temperature inversion: for a given initial humidity, an initially warmer profile will generate a stronger inversion, since the inversion strength is approximately the difference between temperature and dewpoint.

c. The convective regime

The initial dewpoint temperature profiles are slightly unstable at all heights, and increasingly so at higher levels (Figure 5a-c). Cooling by sensible heat transfer to the surface keeps the temperature profiles stable at lower levels, so the cloud must rise to some height (around 750 m in all three cases) before convection can set in. As the cloud enters the convective regime, it deepens substantially (Figure 4a-c) and liquid water path rises sharply (Figure 4d-f). This makes the cloud base lower and thus warmer, while the cloud itself becomes optically thicker. Both these effects help explain the sudden upward jump in downward longwave radiation seen in Figure 3b as the cloud transitions from the stable to the convective regime.

Once in the convective regime, entrainment and mixing provide an additional source of energy to the cloud layer. Cloud temperature could therefore depart substantially from its previous stable-state value, which as argued above is set by the initial air mass dewpoint. It turns out however that the departure is small—a modest cooling of ~2˚C (Figure 5a-c; note that the transition from stable to convective regimes occurs after 1, 2.4 and 3.8 days for T5Hi, T5Lo and T10Lo respectively). As a result, cloud temperature is still to a first approximation controlled by initial dewpoint even in the convective regime.

This behavior can be understood by considering the bulk energetics of the well-mixed sub-cloud layer (Stevens 2006):

$$\frac{ds}{dt} = \frac{E\Delta s - \Delta F_{rad} - F_b}{h}, \quad (3)$$

where s is the liquid-water moist static energy ($s = c_pT + gz - Lq_l$, where c_p is the isobaric specific enthalpy, T is the air temperature, g is the gravitational acceleration, z is the height above the surface, L is the enthalpy of evaporation and q_l is the liquid-water specific humidity) averaged over the depth h of the well-mixed layer (which spans the region between the base of the cloud-top inversion and the top of the surface inversion, Figure 5d-f), E is the entrainment velocity at cloud top, Δs is the jump in s across the cloud-level inversion, $\Delta F_{\rm rad}$ is the net radiative divergence across the layer and F_b is the turbulent heat flux across the bottom of the layer. Neglecting F_b, the ratio $\alpha = E\, \Delta s \,/\, \Delta F_{\rm rad}$ therefore controls the rate at which the layer gains or loses energy: if $\alpha = 1$, s will remain constant at its initial value, while $\alpha < 1$ implies cooling. Observational estimates in subtropical stratocumulus clouds indicate α is typically close to but somewhat smaller than 1 (Stevens 2006). Direct computation in our simulations (Table 1) shows that the same is true here, with α in the range 0.7–0.9 for the three simulations considered. Moreover, the values of *ds/dt* shown in Table 1 imply cooling rates around 0.5–2 K day^{-1}, consistently with the modest cooling of the temperature profiles after entry into the convective regime (Figure 5a-c). We do not compute F_b explicitly, but its magnitude is estimated by the residual of the other terms of the equation, showing this term is generally much smaller than the other terms on the r.h.s. of (3).

Experiment	$\frac{ds}{dt}$	$\frac{E\Delta s}{h}$	$-\frac{\Delta F_{rad}}{h}$	α	Residual
T5Hi (24 – 52 h)	-0.003	0.09	0.10	0.9	0.007
T5Lo (58 – 86 h)	-0.019	0.10	0.14	0.7	0.021
T10Lo (92 – 120 h)	-0.024	0.10	0.14	0.7	0.016

Table 1. Values of the energetic tendency terms for the well-mixed sub-cloud layer in the convective regime, Equation (3) (J kg^{-1} s^{-1}). All terms are averaged over a 28 hour time period after the onset of the convective regime in T5Hi, T5Lo, and T10Lo cases.

5. Surface energy balance and ice temperature evolution

We turn now to atmosphere-sea ice energy exchange and surface temperature evolution in the same three simulations as in the previous section. With the insight into cloud evolution gained there, we can understand the main features of surface temperature and downward longwave evolution shown in Figure 3.

Firstly, Figure 3 shows that following an initial shock—in which the large initial imbalance between atmosphere and surface drives a large upward jump in surface temperature and downward longwave radiation—both T_s and F_{LWd} settle into a general long-term downward trend. This trend can be attributed to the fact that the cloud is rising throughout the simulations, cooling as it follows the initial dewpoint temperature profile (Figure 5d-f). This leads to decreasing longwave emission from the cloud, decreasing F_{LWd} and cooling T_s. Cloud ascent is faster in T5Hi (because of the weaker cloud-top inversion, as discussed in Section 4) than in the other two simulations and thus the downward trend is stronger in that case.

Second, the downward trend discussed above is interrupted by upward jumps coinciding with the transition to the convective regime. As noted in Section 4.3, the cloud becomes thicker in the convective regime, leading to increased F_{LWd}. The different timing of these jumps is because the cloud must rise to some critical height above the surface before convection can set in, so the transition happens earlier the faster the cloud ascends.

Third, and most important, T5Hi has higher F_{LWd} and T_s than the two drier simulations through most of the 5-day duration. We attribute this difference to the higher cloud temperature (at given elevation) in the T5Hi case, due to its higher initial dewpoint temperature. Cloud optical thickness also plays a part, however. For example, during the first simulation day (when all simulations are in the stable state) F_{LWd} is around 30 W m^{-2} higher in T5Hi than in the other two cases (Figure 3b), while its cloud temperature is about 5˚C higher (Figure 5d-f); assuming the cloud emits as a black body, the temperature difference explains around 20 W m^{-2} of the longwave flux difference. The black body assumption is incorrect for the drier cases however, as can be seen by noting that surface net longwave flux $F_{LWnet} = F_{LWd} - F_{LWu}$ is negative in these simulations, with a value around –10 W m^{-2} (Figure 4k,l), despite the fact that surface temperature is considerably colder than cloud base temperature (Figure 5e,f). This implies that the cloud is not fully opaque to longwave radiation, consistent with its modest liquid water path of ~20 g m^{-1} (Shupe and Intrieri 2004), and explains the remaining difference in F_{LWd} between the simulations.

Another notable feature of the simulations is the persistent surface inversion seen in Figure 5d-f. This inversion matches the relatively cold surface temperature—controlled by the surface energy balance (1)—to the warmer air temperature aloft, which is separately controlled by the initial dewpoint temperature. Shear-produced turbulence generates a stable boundary layer that transfers sensible heat down to the surface at a rate of around 5 W m^{-2} on average (Figure 4j-l), with little difference among the three cases.

The conductive flux F_C is initially negative in all three simulations (Figure 4j-l), implying energy flux downward from the surface into the snow layer, and explaining the initial warming of that layer (Figure 4m-o). F_C becomes positive in the latter stages of the simulations: as the cloud rises, F_{LWd} drops and T_s cools, energy initially stored in the snow layer is returned to the atmosphere. The warming of the ice layers below the snow is limited in all cases. T5Hi shows a peak snow warming of around 13˚C, while the ice immediately below warms by only about 5˚C (Figure 4m). These results are quantitatively consistent with the observational results of

Persson et al. (2017; their Fig. 6), providing confidence in our sea ice model. It appears that, given the thermal inertia and conductivity of the ice, the time scale of a single air-mass transformation process is simply too short to allow the deeper ice layers to respond; a rapid succession of similar events would be required to produce deeper effects in the ice, as found observationally by Persson et al. (2017).

6. Conclusions and discussion

We have studied the air-mass transformation process of an initially warm, cloud-free maritime air column in contact with initially cold sea ice under polar night conditions, using an atmospheric LES model coupled to a thermodynamic sea ice model in a set of simulations designed to test the sensitivity to initial air-mass temperature and humidity. We summarize our main results as follows:

- For all initial temperature and humidity conditions considered, a mixed-phase cloud forms initially near the surface and then rises continuously at a rate of several hundred meters per day until it dissipates.
- The cloud passes through two stages during its life cycle: an initial stable, drizzling stratus-like regime, followed by a convective stratocumulus-like regime.
- The initially cold surface warms substantially over the course of the air-mass transformation process. Warming affect the topmost snow layer, but does not penetrate into the deeper sea ice layers; on the 5-day timescale considered, sea ice behaves as a thin slab of modest heat capacity.
- Surface warming is due mostly to surface downward longwave radiation, which depends on the temperature and opacity of the cloud.
- Cloud temperature is constrained to lie close to the initial dewpoint temperature at the same height—the cloud is always a few degrees colder than the initial dewpoint, but this offset changes little along the life cycle. Since the dewpoint depends only on humidity, memory of the initial temperature is lost.

The overarching conclusion is that surface warming over the air-mass transformation process is almost entirely controlled by initial air-mass humidity, regardless of initial temperature. The leading-order mechanism explaining this behavior is that initial humidity controls cloud temperature—via the dewpoint constraint—and cloud temperature controls longwave emission to the surface, which in turn controls surface temperature.

Taken at face value, this mechanism would suggest that surface warming during air-mass transformation should scale as initial dewpoint temperature. This is not the case, however: as shown in Figure 7, surface warming actually increases nonlinearly with initial surface dewpoint temperature (a similar result is obtained using vertically-averaged initial dewpoint temperature).

In fact, increasing initial humidity has additional effects which enhance surface warming above the dewpoint constraint. First, increasing humidity yields clouds with greater liquid water path and thus greater emissivity, enhancing downward longwave radiation particularly for the thin clouds of the stable regime (see discussion in Section 5). Second, increasing humidity extends the lifetime of the convective regime, as is evident comparing Figures 4a and 4b. We have not discussed the mechanisms that dissipate the stratocumulus cloud and terminate the cloud life cycle, which were examined in detail in a previous paper using a similar model framework (Dimitrelos et al. 2020). There, we found that the cloud dissipates when it ascends far enough that air entrained from above is too dry to balance moisture loss by ice crystal precipitation. With a moister initial profile, the cloud can rise higher before it dissipates, lengthening the life cycle.

These additional effects are likely less robust than the dewpoint constraint, and will depend on details of the microphysical processes—particularly cloud depletion by drizzle in the stable regime and by ice crystal precipitation in the convective regime. Nonetheless, in the present set of simulations they result in surface warming scaling roughly linearly with initial humidity (Figure 2a) rather than initial dewpoint.

This linear scaling in humidity has potential implications for polar amplification, or amplification of temperature change over high-latitude land. In a warming climate, marine air masses are expected to warm with roughly constant relative humidity, implying that sea ice or land subject to moist intrusions will warm exponentially following Clausius-Clapeyron scaling. We can quantify this effect by defining an amplification factor $\alpha = \Delta T_s / \Delta T_{d0}$, where ΔT_{d0} and ΔT_s are the quantities plotted in Figure 7, and we note that dewpoint is linear in temperature assuming fixed relative humidity. We find $\alpha = 1.2$ on average across the simulations. Since we expect marine air masses flowing into the poles to warm at roughly the same rate as sea surface temperature (SST) at their origin, a 1˚C warming of midlatitude/subpolar SST would give a typical 1.2˚C surface warming when the air masses move over sea ice or land. This is modest compared to the observed Arctic warming of ~2˚C per degree of midlatitude warming, but could be a contributing factor. If Clausius-Clapeyron scaling continues to hold at higher temperatures, the effect would be larger and could be important in explaining warm winter continental interiors in warm paleoclimates (Cronin and Tziperman 2015).

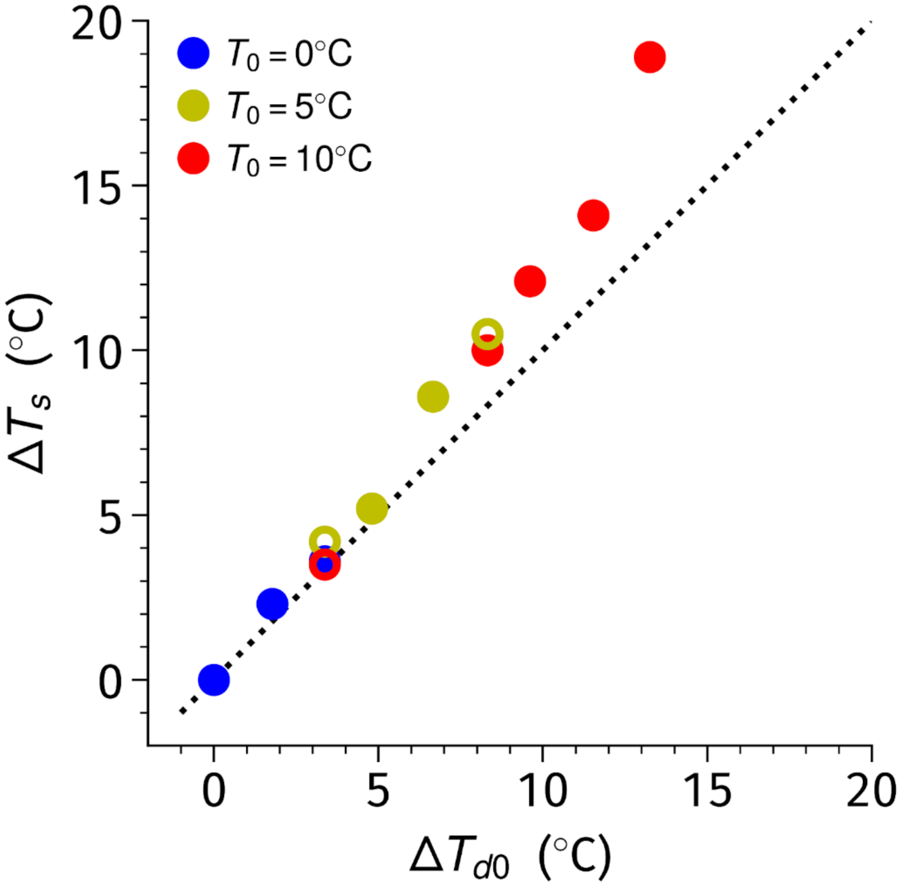

Fig. 7. Time-mean surface temperature T_s as a function of the dewpoint temperature T_{d0} computed from the initial surface specific humidity q_0 (compare with Figure 2a). Values are plotted as differences from the reference case T0RH70. Dotted line is the 1:1 line.

Our results also have implications for the role of atmospheric energy transport in polar amplification. It is common to consider the total moist static energy (MSE) transport as the relevant variable, and to assume that increased MSE convergence into a region will drive surface warming there (e.g. Armour et al. 2019). This implicitly assumes that the dry and moist components of MSE have equal impact on surface warming. Our results suggest however that this equivalence does not hold at the poles, at least in winter: when air masses are advected into the polar region, memory of their original temperature is quickly lost by cloud-top radiation to space and plays little role in determining surface warming. We therefore expect changes in the dry component of MSE convergence to play a minor role in driving surface temperature change compared to the moist component. This expectation is borne out by recent work (Graversen and Burtu 2016, Graversen and Langen 2019) showing that changes in the moist component of polar MSE convergence have a much bigger impact on surface warming than changes in the dry component, in both reanalysis products and climate models. This difference leads to the counterintuitive result that decreased polar MSE convergence contributes to polar warming in a CO_2-doubling climate model experiment (Graversen and Langen 2019).

The climate implications sketched above are necessarily speculative at this point, and future work could explore whether the dewpoint constraint on cloud temperature found here can be identified in reanalysis products and climate models, for instance using Lagrangian tracers to link Arctic clouds to their maritime air masses of origin. Further sensitivity studies using the present modeling framework could study the response to changing the initial temperature and humidity stratification, which could affect the nature and persistence of the clouds, as well as the effects of large-scale subsidence or ascent. In a different direction, the effects of replacing our simple assumptions on cloud condensation and ice nuclei with fully interactive aerosols would be of considerable interest.

Acknowledgments.

The computations were enabled by resources provided by the Swedish National Infrastructure for Computing (SNIC) at the National Supercomputer Centre (NSC) partially funded by the Swedish Research Council through grant agreement no. 2018-05973. This research has partly been supported by the Swedish Science Foundation (Vetenskapsrådet; grant no. 2015-05318) and the Knut and Alice Wallenberg Foundation (grant no. 2015.0162)". We thank Matthew Shupe and Michael Tjernström for useful comments on the paper.

Data availability statement.

The data used in this study is uploaded at the website https://zenodo.org/ with assigned doi: 10.5281/zenodo.6347108. For questions about the model code, please contact annica@misu.su.se.

APPENDIX

Sea ice model

The sea ice model has four homogeneous layers of different density (ρ), heat conductivity (k), specific heat (c), and vertical extent (h). The uppermost layer consists of snow. Below lies a thinner layer of snow which has a higher density and heat conductivity. This layer is named "snow ice" to distinguish it from the snow layer. The snow ice layer has the same specific heat as the layer of snow. Beneath the snow ice layer, two thick ice layers are placed which are distinct from each other due to their different densities and heat conductivities. The first layer is named "soft ice" and its density increases linearly downwards, whereas the opposite applies to its heat conductivity. The bottom layer is called "hard ice" and it has the same heat conductivity as the value at the bottom of the "soft ice" layer. The density, heat conductivity, specific heat, and thickness of snow (snow ice, "soft ice", "hard ice") are denoted as ρ_s (ρ_{si}, ρ_{soft}, ρ_{hard}), k_s (k_{si}, k_{soft}, k_{hard}), c_s (c_{si}, c_{soft}, c_{hard}), and h_s (h_{si}, h_{soft}, h_{hard}). The values of the aforementioned parameters are listed in Table A1. The surface roughness height is set to 0.0004 m, which reflects a flat snow-covered surface (Stull 1988).

<table>
<tr><th>Sea ice layer</th><th>Density
(kg m^{-3})</th><th>Heat conductivity
(W m^{-1} K^{-1})</th><th>Specific heat
(J kg^{-1} K^{-1})</th><th>Thickness
(m)</th></tr>
<tr><td>snow</td><td>350</td><td>0.31</td><td>2090</td><td>0.3</td></tr>
<tr><td>snow ice</td><td>600</td><td>0.5</td><td>2090</td><td>0.15</td></tr>
<tr><td>soft ice
(depth: 0.45 m)</td><td>750</td><td>1</td><td>2108</td><td rowspan="3">0.5</td></tr>
<tr><td>soft ice
(depth: 0.7 m)</td><td>800</td><td>1.5</td><td>2108</td></tr>
<tr><td>soft ice
(depth 0.95)</td><td>850</td><td>2</td><td>2108</td></tr>
<tr><td>hard ice</td><td>900</td><td>2</td><td>2108</td><td>1.5</td></tr>
</table>

Table A1. Characteristics of sea ice model layers.

The time evolution of temperature at layer midpoints and interfaces (9 levels in total, see Figure 1) is computed by integrating the following finite-difference energy transfer equations:

$$F_{LWd} - F_{LWu} + F_{SH} + F_{LH} + F_C + L = 0 \qquad \text{(A1)}$$

$$\rho_s c_s \frac{T_{snow}(t) - T_{snow}(t-dt)}{dt} = k_s \frac{T_{int1} - 2T_{snow} + T_s}{h_s^2} \qquad \text{(A2)}$$

$$k_s \frac{T_{int1} - T_{snow}}{\frac{h_s}{2}} = k_{si} \frac{T_{si} - T_{int1}}{\frac{h_{si}}{2}} \qquad \text{(A3)}$$

$$\rho_{si} c_{si} \frac{T_{si}(t) - T_{si}(t-dt)}{dt} = k_{si} \frac{T_{int2} - 2T_{si} + T_{int1}}{h_{si}^2} \qquad \text{(A4)}$$

$$k_{si} \frac{T_{int2} - T_{si}}{\frac{h_{si}}{2}} = k_{soft} \frac{T_{si} - T_{int2}}{\frac{h_{soft}}{2}} \qquad \text{(A5)}$$

$$\rho_{soft2} c_{soft} \frac{T_{soft}(t) - T_{soft}(t-dt)}{dt} = k_{soft} \frac{T_{int3} - 2T_{soft} + T_{int2}}{h_{soft}^2} \qquad \text{(A6)}$$

$$k_{soft} \frac{T_{int3} - T_{soft}}{\frac{h_{soft}}{2}} = k_{hard} \frac{T_{hard} - T_{int3}}{\frac{h_{hard}}{2}} \qquad \text{(A7)}$$

$$\rho_{hard} c_{hard} \frac{T_{hard}(t) - T_{hard}(t-dt)}{dt} = k_{hard} \frac{T_{bot} - 2T_{hard} + T_{int3}}{h_{hard}^2} \qquad \text{(A8)}$$

$$k_{hard} \frac{T_{bot} - T_{hard}}{\frac{h_{hard}}{2}} = F_W + \rho_{hard} L_f \frac{dh_{hard}}{dt} \qquad \text{(A9)}$$

Here the temperatures in the middle of the snow, snow ice, soft, and hard ice layers are named T_{snow}, T_{si}, T_{soft}, T_{hard}, respectively. T_s is the temperature at the surface while T_{bot} is the temperature at the bottom of the sea ice, which is fixed at the freezing point of salt water (–2˚C). T_{int1}, T_{int2}, and T_{int3} are the temperatures at the interfaces of the snow and the snow ice layer, snow ice and soft ice layers, and soft ice and hard ice layers, respectively. Time is indicated by t, and dt =60 s is the time step. F_W is the net flux of heat from the ocean to the sea ice bottom (Untersteiner et al. 1986) and is set to 2 W m^{-2}. ρ_{soft2} is the density of the soft ice at 0.7 m depth. F_{cbot} in Figure 1a is the term on the l.h.s of equation (A8).

The surface energy flux terms in Equation (A1) include the upward longwave radiative flux $F_{LWu}=\varepsilon\sigma Ts^4$, where ε is the snow emissivity (0.92) and σ is the Stefan-Boltzmann constant; the sensible and latent turbulent fluxes $F_{SH}=\rho_\alpha c_p C_s u(T_a-T_s)$ and $F_{LH}=\rho_\alpha L_v C_e u(q_\alpha-q_s)$ respectively, where the bulk transfer coefficients C_s=1.2·10^{-3} and C_e=0.55·10^{-3} for sensible and latent heat, respectively (Thorpe et al. 1973) and the temperature and specific humidity at the surface and at 15 m altitude, denoted T_s, q_s and T_a, q_a respectively; the surface conductive heat flux $F_C = k_s(\partial T_{snow}/\partial z)_s \approx k_s(T_{snow} - T_s)/(h_s/2)$, and the latent heat involved in surface melting $L = \rho_s L_f (dH/dt)_s \approx \rho_s L_f (H(t)-H(t-dt))/dt$ where the total ice depth $H = h_s + h_{si} + h_{soft} + h_{hard}$. L_v and L_f are the latent heat of vaporization and fusion, respectively.

REFERENCES

Armour, K. C., N. Siler, A. Donohoe, and G. H. Roe, 2019: Meridional atmospheric heat transport constrained by energetics and mediated by large-scale diffusion. *J. Climate*, **32**, 3655–3680, https://doi.org/10.1175/JCLI-D-18-0563.1.

Cronin, T. W., and E. Tziperman, 2015: Low clouds suppress Arctic air formation and amplify high- latitude continental winter warming. *Proceedings of the National Academy of Sciences*, **112**(37), 11490–11495, https://doi.org/10.1073/pnas.1510937112.

Cronin, T. W., H. Li, and E. Tziperman, 2017: Suppression of Arctic air formation with climate warming: Investigation with a two- dimensional cloud- resolving model. *J. Atmos. Sci.*, **74**, 2717–2736, https://doi.org/10.1175/JAS-D-16-0193.1.

Curry, J., 1983: On the formation of continental polar air. *J. Atmos. Sci.*, **40**, 2278–2292, https://doi.org/10.1175/1520-0469(1983)040<2278:OTFOCP>2.0.CO;2.

Curry, J., 1986: Interactions among turbulence, radiation and microphysics in Arctic stratus clouds. *J. Atmos. Sci.*, **43**, 90–106, https://doi.org/10.1175/1520-0469(1986)043<0090:IATRAM>2.0.CO;2.

Curry, J., J. L. Schramm, W. B. Rossow, and D. Randall, 1996: Overview of Arctic cloud and radiation characteristics. *J. Climate*, **9**, 1731–1764, https://doi.org/10.1175/1520-0442(1996)009<1731:OOACAR>2.0.CO;2.

Dimitrelos, A., A. M. L. Ekman, R. Caballero, and J. Savre, 2020: A sensitivity study of Arctic air- mass transformation using large eddy simulation. *J. Geophys. Res. Atmos.*, **125**, e2019JD031738, https://doi.org/10.1029/2019JD031738.

Doyle, J., G. Lesins, C. Thackray, C. Perro, G. Nott, T. Duck, R. Damoah, and J. Drummond, 2011: Water vapor intrusions into the High Arctic during winter. *Geophys. Res. Lett.*, **38**, L12806, https://doi.org/10.1029/2011GL047493.

Fu, Q., and K.-N. Liou, 1993: Parameterization of the radiative properties of cirrus clouds, *J. Atmos. Sci.*, **50**, 2008–2025, https://doi.org/10.1175/1520-0469(1993)050<2008:POTRPO>2.0.CO;2.

Garratt, J. R., 1994: *The Atmospheric Boundary Layer*, pp. 49–60, chap. 3.3, Cambridge University Press, Cambridge, U. K.

Gong, T., S. Feldstein, and S. Lee, 2017: The role of downward infrared radiation in the recent Arctic winter warming trend. *J. Climate*, **30**, 4937–4949, https://doi.org/10.1175/JCLI-D-16-0180.1.

Goosse, H., and Coauthors, 2018: Quantifying climate feedbacks in polar regions. *Nat. Commun.*, **9**, 1919, https://doi.org/10.1038/s41467-018-04173-0.

Graversen, R. G., and P. L. Langen, 2019: On the role of the atmospheric energy transport in 2xCO2–induced polar amplification in CESM1. *J. Climate*, **32**, 3941–3956, https://doi.org/10.1175/JCLI-D-18-0546.1.

Graversen, R. G., and M. Burtu, 2016: Arctic amplification enhanced by latent energy transport of atmospheric planetary waves. *Quart. J. Roy. Meteorol. Soc*, **142**, 2046–2054, https://doi.org/10.1002/qj.2802.

Kay, J. E., T. L'Ecuyer, H. Chepfer, N. Loeb, A. Morrison, and G. Cesana 2016: Recent advances in Arctic cloud and climate research. *Curr. Clim. Change Rep.*, **2**, 159–169, https://doi.org/10.1007/s40641-016-0051-9.

Khvorostyanov, V. I., and J. Curry 2005: Fall velocities of hydrometeors in the atmosphere: Refinements to a continuous analytical power law, *J. Atmos. Sci*., **62**, 4343– 4357, https://doi.org/10.1175/JAS3622.1.

Li, Z., and K.-M. Xu, 2020: Arctic clouds simulated by a multiscale modeling framework and comparisons with observations and conventional GCMs. *J. Geophys. Res. Atmos.*, **125**, e2019JD030522, https://doi.org/10.1029/2019JD030522.

Mellado, J. P., 2017: Cloud-top entrainment in stratocumulus clouds. *Ann. Rev. Fluid Mech*., **49**, 145–169, https://doi.org/10.1146/annurev-fluid-010816-060231.

Messori, G., C. Woods, and R. Caballero, 2018: On the drivers of wintertime temperature extremes in the High Arctic. *J. Climate*, **31**, 1597–1618, https://doi.org/10.1175/JCLI-D-17-0386.1.

Morrison, H., and W. Grabowski 2008: Modeling supersaturation and subgrid-scale mixing with two-moment bulk warm microphysics, *J. Atmos. Sci.*, **65**, 792–812, https://doi.org/10.1175/2007JAS2374.1.

Morrison, H., and Coauthors, 2011: Intercomparison of cloud model simulations of Arctic mixed- phase boundary layer clouds observed during SHEBA/FIRE- ACE, *J. adv. model. earth syst.*, **3**, M06003, https://doi.org/10.1029/2011MS000066.

Morrison, H., G. de Boer, G. Feingold, J. Harrington, M. Shupe, and K. Sulia, 2012: Resilience of persistent Arctic mixed-phase clouds. *Nature Geoscience*, **5**, 11–17, https://doi.org/10.1038/ngeo1332.

Park, D.-S. R., S. Lee, and S. B. Feldstein, 2015: Attribution of the recent winter sea ice decline over the Atlantic sector of the Arctic Ocean. *J. Climate,* **28**, 4027–4033, https://doi.org/10.1175/JCLI-D-15-0042.1.

Park, H.-S., S. Lee, S.-W. Son, S. B. Feldstein, and Y. Kosaka, 2015: The impact of poleward moisture and sensible heat flux on Arctic winter sea ice variability. *J. Climate*, **28**, 5030–5040, https://doi.org/10.1175/JCLI-D-15-0074.1.

Persson, P. O. G., M. D. Shupe, D. Perovich, and A. Solomon, 2017: Linking atmospheric synoptic transport, cloud phase, surface energy fluxes, and sea- ice growth: Observations of midwinter SHEBA conditions. *Clim. Dyn.*, **49**(4), 1341–1364, https://doi.org/10.1007/s00382- 016- 3383- 1.

Pithan, F., B. Medeiros, and T. Mauritsen, 2014: Mixed- phase clouds cause climate model biases in Arctic wintertime temperature inversions. *Clim. Dyn*, **43**(1–2), 289–303, https://doi.org/10.1007/s00382- 013- 1964- 9.

Pithan, F., and Coauthors, 2016: Select strengths and biases of models in representing the Arctic winter boundary layer over sea ice: the Larcform 1 single column model intercomparison, *J. adv. model. earth syst.*, **8**, 1345–1357, https://doi.org/10.1002/2016MS000630.

Pithan, F., and Coauthors, (2018): Role of air-mass transformations in exchange between the Arctic and mid-latitudes. *Nature Geosci.*, **11**, 805-812, https://doi.org/10.1038/s41561-018-0234-1.

Previdi, M., K. L. Smith, and L. M. Polvani, 2021: Arctic amplification of climate change: a review of underlying mechanisms. *Environ. Res. Lett.*, **16**, 093003, https://doi.org/10.1088/1748-9326/ac1c29.

Pruppacher, H. R., and J. D. Klett 1997: *Microphysics of Clouds and Precipitation*, 2nd ed., pp. 51–61 (chap. 2); 442–443 (chap. 10); 502–567 (chap. 13), Kluwer Acad., Norwell, Mass.

Savre, J., A. M. L. Ekman, and G. Svensson, 2014: Technical note: Introduction to MIMICA, a large-eddy simulation solver for cloudy planetary boundary layers. *J. adv. model. earth syst.*, **6**(3), 630-649, https://doi.org/10.1002/2013MS000292.

Seifert, A., and K. Beheng, 2006: A two-moment cloud microphysics parameterization for mixed-phase clouds. Part 1: Model description. *Meteorol. Atmos. Phys.*, **92**, 45–66, https://doi.org/10.1007/s00703-005-0112-4.

Shupe, M., 2011: Clouds at Arctic atmospheric observatories. Part 2: Thermodynamic phase characteristics. *J. Appl. Meteorol. Climatol.*, **50**, 645–661, https://doi.org/10.1175/2010JAMC2468.1.

Shupe, M. D., and J. M. Intrieri, 2004: Cloud radiative forcing of the Arctic surface: The influence of cloud properties, surface albedo, and solar zenith angle. *J. Climate*, **17**, 616–628. https://doi.org/10.1175/1520-0442(2004)017<0616:CRFOTA>2.0.CO;2.

Shupe, M. D., P. O. G. Persson, I. M. Brooks, M. Tjernström, J. Sedlar, T. Mauritsen, S. Sjogren, and C. Leck, 2013: Cloud and boundary layer interactions over the Arctic sea ice in late summer, *Atmospheric Chem. Phys.*, **13**, 9379–9399, https://doi.org/10.5194/acp-13-9379-2013.

Solomon, A., M. D. Shupe, P. O. G. Persson, and H. Morrison, 2011: Moisture and dynamical interactions maintaining decoupled Arctic mixed-phase stratocumulus in the presence of a humidity inversion, *Atmospheric Chem. Phys.*, **11**, 10127–10148, https://doi.org/10.5194/acp-11-10127-2011.

Sotiropoulou, G., and Coauthors, 2016: Atmospheric conditions during the Arctic Clouds in Summer Experiment (ACSE): Contrasting open water and sea ice surfaces during melt and freeze-up seasons. *J. Climate*, **29**, 8721–8744, https://doi.org/10.1175/JCLI-D-16-0211.1.

Stevens, B., 2006: Bulk boundary-layer concepts for simplified models of tropical dynamics. *Theor. Comput. Fluid Dyn.*, **20**, 279–304, https://doi.org/10.1007/s00162-006-0032-z.

Stramler, K., A. D. D. Genio, and W. B. Rossow, 2011: Synoptically driven Arctic winter states. *J. Climate,* **24**, 1747–1762, https://doi.org/10.1175/2010JCLI3817.1.

Svensson, G., and T. Mauritsen, 2020: Arctic cloud systems. *Clouds and Climate: Climate Science's Greatest Challenge,* Cambridge University Press.

Thorpe, S.A, 1973: Turbulence in stably stratified fluids: A review of laboratory experiments. *Bound.-Layer Meteorol.*, **5**, 95–119, https://doi.org/10.1007/BF02188314.

Wexler, H., 1936: Cooling in the lower atmosphere and the structure of polar continental air. *Mon. Wea. Rev*, **64**, 122–136, https://doi.org/10.1175/1520-0493(1936)64<122:CITLAA>2.0.CO;2.

Woods, C., R. Caballero, and G. Svensson, 2013: Large-scale circulation associated with moisture intrusions into the Arctic during winter. *Geophys. Res. Lett.*, **40**, 4717–4721, https://doi.org/10.1002/grl.50912.

Woods, C., and R. Caballero, 2016: The role of moist intrusions in winter Arctic warming and sea ice decline. *J. Climate*, **29**, 4473–4485, https://doi.org/10.1175/JCLI-D-15-0773.1.

You, C., M. Tjernström, and A. Devasthale, 2021: Eulerian and Lagrangian views of warm and moist air intrusions into summer Arctic. *Atmos. Res.*, **256**, 105586, https://doi.org/10.1016/j.atmosres.2021.105586.